HiExM: high-throughput expansion microscopy enables scalable super-resolution imaging

John H. Day[1], Catherine Marin Della Santina[1#], Pema Maretich[2#], Alexander L. Auld[2#], Kirsten K. Schnieder[2], Tay Shin[3], Edward S. Boyden[1,3,4,5,6,7,8,9], Laurie A. Boyer[1,2,9*]

[1]Department of Biological Engineering, [2]Department of Biology, [3]Department of Media Arts and Sciences, [4]Department of Brain and Cognitive Sciences, [5]McGovern Institute, [6]Howard Hughes Medical Institute, [7]K Lisa Yang Center for Bionics, [8]Center for Neurobiological Engineering, [9]Koch Institute, Massachusetts Institute of Technology, 77 Massachusetts Avenue, Cambridge, MA 02139 USA

#These authors contributed equally.

*Correspondences:
Laurie A. Boyer
lboyer@mit.edu
Tel: +1 617 324-3335

Key words: expansion microscopy, high-throughput, nanoscopy, super-resolution imaging

1

Abstract

Expansion microscopy (ExM) enables nanoscale imaging using a standard confocal microscope through the physical, isotropic expansion of fixed immunolabeled specimens. ExM is widely employed to image proteins, nucleic acids, and lipid membranes in single cells at nanoscale resolution; however, current methods cannot be performed in multi-well cell culture plates which limits the number of samples that can be processed simultaneously. We developed High-throughput Expansion Microscopy (HiExM), a robust platform that enables expansion microscopy of cells cultured in a standard 96-well plate. Our method enables consistent ~4.2x expansion within individual wells, across multiple wells, and between plates processed in parallel. We also demonstrate that HiExM can be combined with high-throughput confocal imaging platforms greatly improve the ease and scalability of image acquisition. As an example, we analyzed the effects of doxorubicin, a known cardiotoxic agent, in human cardiomyocytes (CMs) based on Hoechst signal intensity. We show a dose dependent effect on nuclear chromatin that is not observed in unexpanded CMs, suggesting that HiExM improves the detection of cellular phenotypes in response to drug treatment. Our method broadens the application of ExM as a tool for scalable super-resolution imaging in biological research applications.

Significance Statement

Expansion microscopy (ExM) is a flexible, highly accessible, and widely implemented technique for super-resolution imaging of fixed biological specimens. For many ExM users, slide-based sample preparation and manual imaging limit the total volume of data generated and the number of conditions that are tested in parallel. In this work, we develop a simple and inexpensive device that allows the user to perform ExM within the wells of a 96-well plate. We show that samples prepared with our workflow can be imaged with a high-throughput autonomous confocal microscope, allowing for scalable super-resolution image acquisition. Our device retains the accessibility of ExM while extending the application space of ExM to problems that require the analysis of many conditions, treatments, and time points.

Main Text

The ability to resolve subcellular features can greatly enhance biological discovery, identification of disease targets, and the development of targeted therapeutics. Super-resolution microscopy methods such as structured illumination microscopy (SIM), electron microscopy (EM), stochastic optical reconstruction microscopy (STORM) and photoactivated localization microscopy (PALM) enable nanoscale imaging of specimens.[1–3] However, these approaches require specialized, costly reagents and microscopes. Expansion microscopy (ExM) is an inexpensive and accessible method that similarly resolves fluorescently labeled structures at subcellular resolution by isotropically enlarging specimens within a swellable polyelectrolyte hydrogel.[4] Images of expanded cells show a higher effective resolution due to an increase in the distance between the fluorescent molecules beyond the Rayleigh limit typical of a conventional confocal microscope. Super-resolution imaging and ExM are critical tools that are widely used in biological research; however, processing and sample imaging requires time consuming manual manipulation limiting its throughput. Although there has been success in increasing the throughput of certain super-resolution microscopy techniques, these methods still require highly specialized equipment and expertise which limits their application.[5–8] To broaden the utility and ease of use of super-resolution imaging, we developed High-Throughput Expansion Microscopy (HiExM) that combines parallel sample processing and automated high-content confocal imaging in a standard 96-well cell culture plate.

Adapting standard ExM to a 96-well plate requires the reproducible delivery of a small volume of gel solution to each well (<1 µL compared to ~200 µL/sample for classical ExM). This small volume allows complete gel expansion within the size constraints of wells in a 96-well plate. To achieve this goal, we engineered a device that retains small liquid droplets when dipped into a reservoir of monomeric expansion gel solution. These droplets can then be deposited into the centers of multiple wells of the culture plate (**Figs. 1a,b**). The retention of the gel solution is mediated by a series of reticulated grooves at the end of a cylindrical post which favors the formation of a pendant droplet (**Fig. 1c**). We estimate that each post retains ~230 nL of gel solution as measured by the mass of liquid accumulated on all post tips of a single device after dipping (Supplementary Methods).

The small volume of gel solution delivered by the device in each well forms a toroid where the inner surface is molded by the conical surface of the post-tip and the outer surface is constrained

3

by surface tension (**Figs. 1c,d**). As such, the post-tip dimensions were designed to deliver a volume of gel solution that would maximally expand to the diameter of the well (**Fig. 1d**). The toroidal gel allows for isotropic gel expansion within the well constraints while allowing for easy device removal because the inner surface of the gel expands outward away from the conical post-tip, effectively detaching the gel from the device. To achieve this toroidal geometry, we incorporated a compliant mechanism composed of three key features that allows each post of the device to contact the midpoint at the bottom of a well (**Fig. S1**). First, two sets of three cantilevers (termed 'pressure struts') are located at each end of the device while the remainder consists of two rows of 6 posts (12 posts per device). These pressure struts apply outward force to the inside of the outer four wells ensuring that the device remains in contact with the well surface throughout the expansion process. Second, the spine of the device incorporates several notches extending through the long side of the device allowing it to bend to accommodate inconsistencies between the depths of individual wells. Finally, the post lengths are offset from the center four posts out to allow for sequential deformation that ensures each post contacts the well surface. Together, these design features allow for reproducible deposition and expansion of gels in a 96-well plate.

To test our device for high-throughput gel expansion, we first performed standard expansion microscopy using ammonium persulfate (APS) and tetramethylethylenediamine (TEMED) to initiate gel polymerization (**Fig. S2a**).[9] Since APS rapidly accelerates polymerization of polyacrylamide hydrogels, TEMED-containing expansion gel solution is first delivered by the device and removed leaving a ≤1µl droplet in each well of the plate on ice. A second device is then used to deliver APS-containing expansion gel solution at the same volume and the polymerization reaction is initiated by exposing the plate to heat. Given the large air-liquid-interface in the well plate, droplet delivery and polymerization are performed in a nitrogen filled glove bag to minimize oxygen inhibition of the reaction. Although we observed gel formation across wells, polymerization and expansion were inconsistent, likely due to inhomogeneous radical formation and rapid evaporation relative to the rate of polymerization (**Movie S1**). To overcome this limitation, we tested photochemical initiators including Lithium phenyl(2,4,6-trimethylbenzoyl)phosphinate (LAP), diphenyl(2,4,6-trimethylbenzoyl)phosphine oxide (TPO), and 1-[4-(2-Hydroxyethoxy)-phenyl]-2-hydroxy-2-methyl-1-propane-1-one (Irgacure 2959) which have been used to control polymerization of polyacrylamide gels when exposed to UV light.[10,11] LAP has previously shown success in slide-based ExM using PEG-based hydrogels.[12,13] We

found that using Irgacure 2959 resulted in highly reproducible gel formation and expansion (**Movie S2**) in our platform compared to other photoinitiators tested or standard ExM chemistry.

We next tested whether our HiExM platform could achieve nanoscale image resolution of biological specimens. Briefly, A549 cells were cultured, fixed, permeabilized and immunostained with alpha-tubulin antibodies to visualize microtubules as a reference structure before and after expansion. Stained samples were then incubated with Acryloyl-X (AcX) overnight at 4ºC to allow anchoring of native proteins to the polymer matrix during gel formation. Device posts were immersed in the expansion gel solution containing 0.1% Irgacure 2959. The devices were then inserted into the well plate followed by exposure to UV light (365nm) in an anoxic environment to initiate the polymerization reaction. Cells embedded in the resulting gels were digested with Proteinase K then expanded in deionized water overnight (**Fig. S2a**; see Methods). Visual inspection using an epifluorescence microscope indicated both robust gel formation and fluorescence signal retention across wells. Although we observed bleaching of AlexaFluor$^{®}$ dyes in our photopolymerized gels initiated with Irgacure 2959, Cyanine-based Fluorescent (CF$^{®}$) dyes are robust against bleaching in HiExM and result in reproducible signal retention (**Fig. S3**).[14]

A major workflow bottleneck associated with super-resolution imaging, including current ExM protocols, is the significant time and expertise required for image acquisition. For example, the vertical component of expansion makes it difficult to image the full depth of the sample. Moreover, expansion gels are not bound to the well surface following digestion in our system, which requires increasing the search space for planar coordinates and focal depths to fully image the expanded specimen. To enable rapid 3D image capture of expanded cells in 96-well plates, we used a high content confocal microscope (Opera Phenix system, Perkin Elmer) (**Fig. 2a**). This approach allowed autonomous capture of images across the entire plate at a resolution of ~115 nm compared to ~463 nm for unexpanded samples with the same microscope, objective (63X, 1.15NA water immersion), and imaging wavelength (**Fig. S4**).

We next benchmarked the performance of our platform relative to slide-based proExM.[9] Image distortion due to expansion was measured using a non-rigid registration (NRR) algorithm.[4] Prior to expansion, images of stained A549 cells were acquired using the Opera Phenix from 61 fields around the center of each gel (**Fig. 2a**). Cells were then expanded as described above and 12

5

fields were imaged per well. Distortion was calculated using the root mean squared error (RMSE) of a 2-dimensional deformation vector field by comparing microtubule morphology in the same cell(s) before and after expansion in six to ten fields in each well across six arbitrarily selected wells (**Figs. 2c,d**). The average percent error (up to 40 µm measurement length post-expansion) was plotted against the distance from the center of the gel (**Fig. 2e**). Our analysis found no correlation (R^2 = 0.003) between expansion error and distance from the gel center. In fact, we observed only a single or small number of outliers (>3 s.d.) in any given well (<2 instances per gel of 6 gels tested). These outliers are not expected to affect biological interpretation. These outliers, which are closer to the center of the gel, likely occur when the device post is not in full contact with the well surface, resulting in a higher volume of gel at the center of the toroid that resists gel swelling under the device (**Fig. S5**). Expansion was also highly consistent when comparing wells across multiple plates, showing minimal error (average = 3.68%), comparable to slide-based ExM (**Fig. 2f**).[4,9] In fact, we observed only a small number of image fields (7 of 58) with average percent error above 6% (maximum 6.78%). Moreover, calculated error across gels using APS and TEMED polymerization chemistry showed that photoinitiation resulted in markedly lower spatial errors in our platform (**Fig. S6**). Analyzing cell seeding densities also showed that cell confluency did not affect image distortion as measured by NRR (**Fig. S7**).

Finally, we measured expansion factors within individual gels, between gels, and across plates by manually measuring the distance between pairs of cell landmarks in FIJI before and after expansion. We found that the expansion factor was highly reproducible across different regions of the gel confirming robust expansion using our method (**Fig. 2g**). Moreover, the average expansion factor of wells sampled across three plates was 4.16 +/- 0.394 (**Fig. 2h**), consistent with proExM.[9] It is important to note that the expansion factor, while uniform within gels, is somewhat variable between gels and plates. This should be taken into consideration for studies where absolute length measurements are important. Collectively, these data show that our HiExM method results in reproducible nanoscale and isotropic expansion of cells within gels, across wells and plates.

The ability to image cells at increased resolution using HiExM provides an opportunity to analyze nanoscale cellular features for a range of applications including cell phenotyping as well as drug and toxicology studies. As proof of concept, we analyzed the effects of doxorubicin (dox), a potent chemotherapeutic that is known to impair cardiac function in some patients, on human

induced pluripotent stem cell derived cardiomyocytes (CMs) cultured in 96 well plates (**Fig. 3a**).[15] Commonly used dox concentrations in *in vitro* cardiotoxicity studies involving CMs fall within the range of 0.1 μM to 10 μM, with specific concentrations depending on experimental goals[16–19]. Although studies largely focus on electrophysiology, structural changes at the cellular level also provide critical information. For example, changes in nuclear DNA damage, size, shape, and morphology can be indicative of cellular stress or damage, which is commonly observed at high dox doses (>200 nM) in *in vitro* studies.[16–20] However, heart tissue is exposed to a wide range of dox concentrations in clinical treatments.[15,21,22] Because HiExM has the sensitivity to detect nanoscale cellular features, we Hoechst stained CM nuclei treated with 1 nM, 10 nM, 100 nM, and 1 μM dox for 24 hours compared with DMSO (**Fig 3b**). Although we did not observe a significant change in nuclear volume (data not shown), images showed increasing Hoechst density at the nuclear periphery in a dox concentration dependent manner.

To gain further insights, we quantified the gradient slope of Hoechst intensity across the nuclear periphery. To this end, we masked 529 nuclei from background in dox treated and control samples and selected single optical sections by identifying the center of the nucleus in the z axis (**Fig 3c**). To account for irregular nuclear shapes, we iteratively group pixels into rings for each nucleus starting with the edge of the mask (**Fig 3d**). The mask is dilated outward from the edge of the nucleus to include a background reading as reference. The average pixel intensity value for each ring represents the average Hoechst intensity as a function of relative distance from the edge of the nucleus to its center (**Fig 3e, Movie S3**). Notably, HiExM revealed a peak of Hoechst intensity at the edge of the nucleus that is not observed pre-expansion (**Fig 3f**). A line scan-based analysis showed the same trend (**Fig S8**). To further evaluate these differences, we next calculated the first derivative of each curve and found the maximum and minimum values, which correspond to the gradient slopes on either side of the peak (**Fig 3g, Fig S9**). In this case, a higher magnitude of gradient slope reflects a 'sharper' transition from the nuclear edge to the background (outside) or from the nuclear edge to the nucleoplasm (inside). Post-expansion, the gradient slopes at both sides of the peak show a significant increase at dox concentrations as low as 10 nM compared to DMSO, whereas no trend is observed pre-expansion (**Fig 3g**).

In addition to gradient slopes at the nuclear edge, we also quantified the pattern of Hoechst signal at the nuclear edge by calculating the curvature of the peak using the second derivative (**Fig 3h**). These data also show a significant increase in Hoechst intensity at 10 nM dox compared to

7

DMSO, whereas no significant difference is observed using conventional confocal microscopy (**Fig 3i**). We note that, for both the outer gradient slope and peak curvature, values decrease from 100 nM to 1 µM dox, consistent with increased chromatin condensation associated with apoptosis typically observed at higher dox concentrations[18,23]. In contrast, CMs treated with increasing concentrations of H_2O_2, another cellular stressor, did not show altered Hoechst patterns using the same dox treatment regimen (**Fig S10**). Overall, our analysis demonstrates the ability of HiExM to detect subtle phenotypic changes compared to standard confocal microscopy that could improve drug screening approaches.

HiExM is a simple and inexpensive method that increases the throughput of expansion microscopy, greatly extending the applications for nanoscale imaging. The compatibility of HiExM with standard cell culture practices is a key advantage of our approach over other approaches that increase ExM throughput.[8] Here, we developed a photo-active gel formula based on proExM for expansion in our HiExM workflow; however, our platform is amenable to other photo-active expansion chemistries that do not require CF dyes (**Fig S11**)[13]. HiExM is also compatible with autonomous imaging, allowing imaging and data acquisition of thousands of cells in a day. Moreover, our device is fabricated with CNC milling, a common fabrication technique available in most academic settings, making our technology widely accessible. Our HiExM device can also be produced by injection molding which can further extend its accessibility and distribution. Our device design can also be adapted to cell culture plates of varying dimensions including a 24 well plate which accommodates chemistries to further increase expansion factor (**Fig S12**).[24] Taken together, HiExM facilitates quantitative super-resolution-based screening and discovery approaches with broad biological and pharmaceutical applications by increasing the number of samples that can be processed in parallel.

References

1. Heintzmann, R. & Huser, T. Super-Resolution Structured Illumination Microscopy. *Chem. Rev.* **117**, 13890–13908 (2017).

2. Egerton, R. F. *Physical Principles of Electron Microscopy*. (Springer International Publishing, 2016). doi:10.1007/978-3-319-39877-8.

3. Henriques, R., Griffiths, C., Hesper Rego, E. & Mhlanga, M. M. PALM and STORM: Unlocking live-cell super-resolution. *Biopolymers* **95**, 322–331 (2011).

4. Chen, F., Tillberg, P. W. & Boyden, E. S. Expansion microscopy. *Science* **347**, 543 (2015).

5. Holden, S. J. *et al.* High throughput 3D super-resolution microscopy reveals *Caulobacter crescentus* in vivo Z-ring organization. *Proc. Natl. Acad. Sci.* **111**, 4566–4571 (2014).

6. Gunkel, M., Flottmann, B., Heilemann, M., Reymann, J. & Erfle, H. Integrated and correlative high-throughput and super-resolution microscopy. *Histochem. Cell Biol.* **141**, 597–603 (2014).

7. Mahecic, D. *et al.* Homogeneous multifocal excitation for high-throughput super-resolution imaging. *Nat. Methods* **17**, 726–733 (2020).

8. Xie, J. *et al.* An Image-Based High-Throughput and High-Content Drug Screening Method Based on Microarray and Expansion Microscopy. *ACS Nano* acsnano.3c01865 (2023) doi:10.1021/acsnano.3c01865.

9. Tillberg, P. W. *et al.* Protein-retention expansion microscopy of cells and tissues labeled using standard fluorescent proteins and antibodies. *Nat. Biotechnol.* **34**, 987–992 (2016).

10. Li, N., Xiang, Z., Rong, Y., Zhu, L. & Huang, X. 3D Printing Tannic Acid-Based Gels via Digital Light Processing. *Macromol. Biosci.* **22**, 2100455 (2022).

11. Pawar, A. A. *et al.* High-performance 3D printing of hydrogels by water-dispersible photoinitiator nanoparticles. *Sci. Adv.* **2**, e1501381 (2016).

12. Blatchley, M. R. *et al.* In Situ Super-Resolution Imaging of Organoids and Extracellular Matrix Interactions via Phototransfer by Allyl Sulfide Exchange-Expansion Microscopy (PhASE-ExM). *Adv. Mater.* **34**, 2109252 (2022).

13. Günay, K. A. *et al.* Photo-expansion microscopy enables super-resolution imaging of cells embedded in 3D hydrogels. *Nat. Mater.* **22**, 777–785 (2023).

14. Jiang, J., Li, X., Mao, F., Wu, X. & Chen, Y. Small molecular fluorescence dyes for immuno cell analysis. *Anal. Biochem.* **614**, 114063 (2021).

15. Johnson-Brbor, K. & Dubey, R. *Doxorubicin*. (StatPearls Publishing, 2023).

16. Maillet, A. *et al.* Modeling Doxorubicin-Induced Cardiotoxicity in Human Pluripotent Stem Cell Derived-Cardiomyocytes. *Sci. Rep.* **6**, 25333 (2016).

17. Yu, X. *et al.* Dexrazoxane Protects Cardiomyocyte from Doxorubicin-Induced Apoptosis by Modulating miR-17-5p. *BioMed Res. Int.* **2020**, 1–11 (2020).

18. Zhao, L. & Zhang, B. Doxorubicin induces cardiotoxicity through upregulation of death receptors mediated apoptosis in cardiomyocytes. *Sci. Rep.* **7**, 44735 (2017).

19. Stefanova, M. E. *et al.* Doxorubicin Changes the Spatial Organization of the Genome around Active Promoters. *Cells* **12**, 2001 (2023).

20. Gewirtz, D. A critical evaluation of the mechanisms of action proposed for the antitumor effects of the anthracycline antibiotics adriamycin and daunorubicin. *Biochem. Pharmacol.* **57**, 727–741 (1999).

21. Chao, F.-C., Manaia, E. B., Ponchel, G. & Hsieh, C.-M. A physiologically-based pharmacokinetic model for predicting doxorubicin disposition in multiple tissue levels and quantitative toxicity assessment. *Biomed. Pharmacother.* **168**, 115636 (2023).

22. Greene, R. F., Collins, J. M., Jenkins, J. F., Speyer, J. L. & Myers, C. E. Plasma Pharmacokinetics of Adriamycin and Adriamycinol: Implications for the Design of in Vitro Experiments and Treatment Protocols. (1983).

23. Toné, S. *et al.* Three distinct stages of apoptotic nuclear condensation revealed by time-lapse imaging, biochemical and electron microscopy analysis of cell-free apoptosis. *Exp. Cell Res.* **313**, 3635–3644 (2007).

24. Damstra, H. G. *et al.* Visualizing cellular and tissue ultrastructure using Ten-fold Robust Expansion Microscopy (TREx). *eLife* **11**, e73775 (2022).
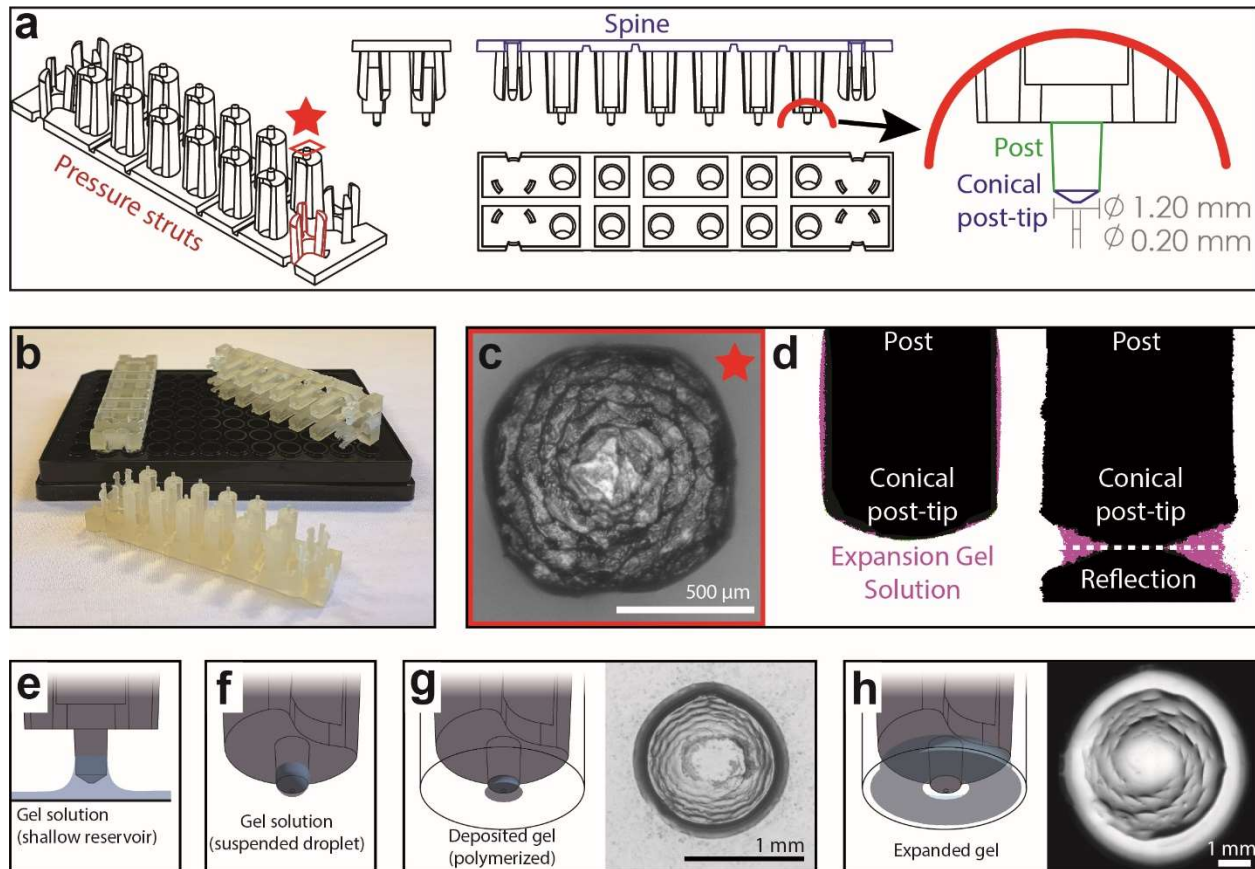
Figures

Fig. 1. HiExM enables gel formation and expansion in a 96-well cell culture plate. a. Schematic representation of HiExM devices showing the key features highlighted in color. **b.** Example devices used in 96-well cell culture plates. The device on the left is inserted into the well plate. **c.** Brightfield image of the conical post-tip shows the pattern of grooves that mediate fluid retention. **d.** Fluid retention at the conical post-tip of the device. Silhouettes taken by an optical comparator of the profile of a single post suspended above a surface (left) and in contact with a surface (right) show a fluid droplet interacting with the device. Upon device insertion, the gel solution fills the space under the conical post tip, forming the toroid gel. **e-h.** Schematic of HiExM gel deposition and expansion workflow. **e.** The device is immersed in a shallow reservoir of gel solution. **f.** Upon removal, the tip of each device post retains a small volume of gel solution. **g.** Gel solution is deposited by the device into the centers of each well of the cell culture plate. Brightfield image (right) shows gel geometry and size prior to expansion. Note that gels deposited in HiExM cover ~1.1 mm^2 of the cell culture surface to accommodate for expansion, and do not

include cells outside the gel footprint. **h.** Polymerization and expansion are carried out with the device in place. Brightfield image (right) shows gel geometry and size after expansion.
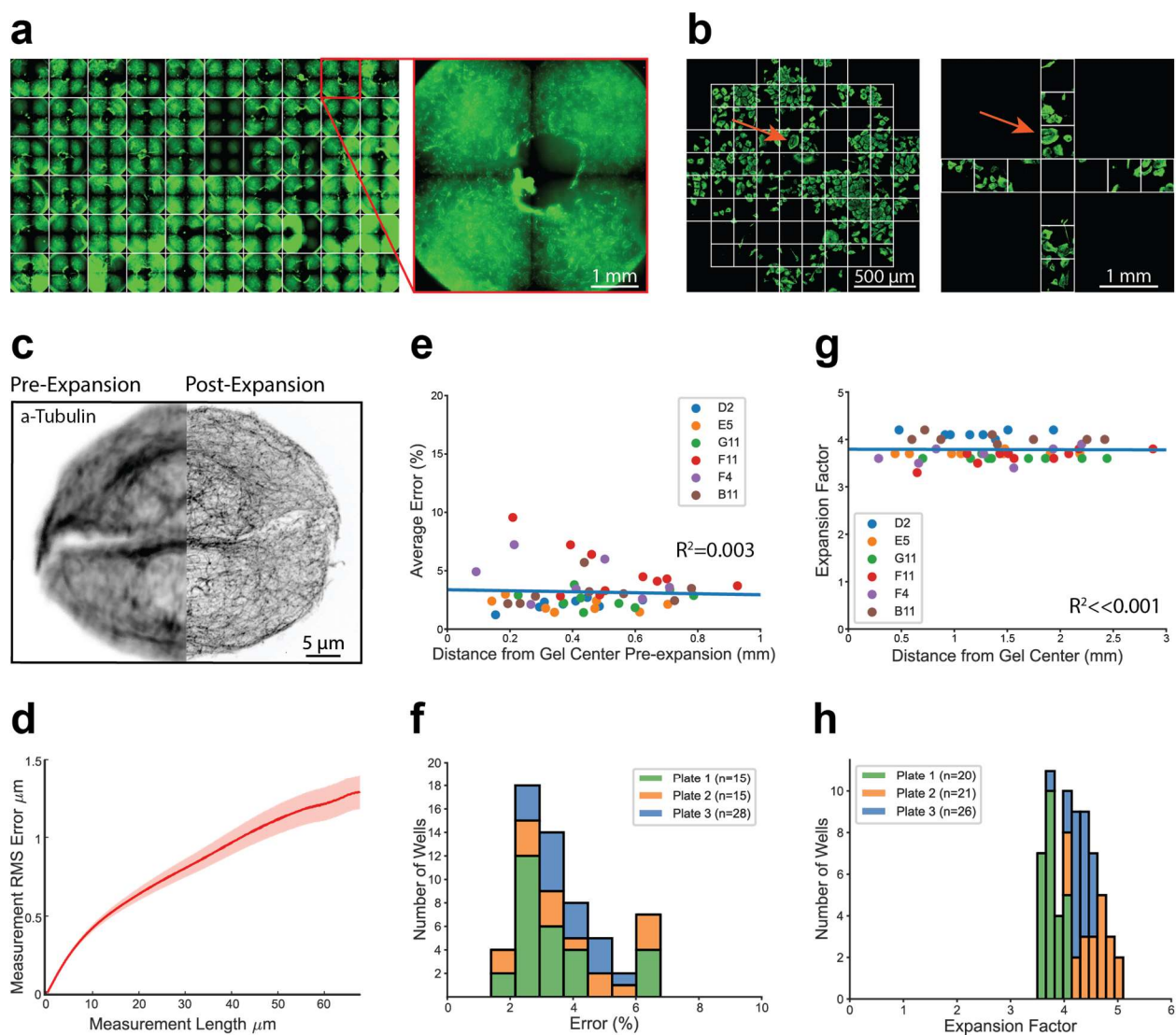

Fig. 2. HiExM is compatible with nanoscale expansion and automated image acquisition of human cells with minimal distortion. a. Expanded gels in a 96 well plate imaged at 5x with an inset showing an individual gel. **b.** Imaging fields for pre-expansion and post-expansion data acquisition. Prior to expansion, 61 fields were imaged at 63x around the center of the gel. After expansion, 12 fields were imaged at 20x magnification. Max projections for each field were then stitched together and manually inspected to identify fields in the pre-expansion and post-expansion image sets containing matching cells. Arrows show an example of a field representing the same pair of cells before and after expansion. **c.** Representative registered fluorescence

12

image of microtubules before (left) and after (right) expansion showing the increase in resolution conferred by expansion. **d.** Representative error curve calculated using non-rigid registration on 43 independent fields of view. The shaded region denotes one standard error of the mean. **e.** Error is not dependent on the location of a given field of view within the gel. Each data point represents the average percent error (up to 40 μm measurement length post-expansion) for a given field of view as determined by an NRR analysis. Six wells were analyzed in seven to ten fields of view. The distance from the center of each field of view to the center of the well was measured manually in FIJI using the stitched pre-expansion image set. **f.** Stacked-bar histogram showing the distribution of average error among gels across three plates (average = 3.63% +/- 1.39). Average error percentages for each well plate: 3.73 +/- 0.879, 3.89 +/- 1.65, and 3.43 +/- 1.44. **g.** Expansion factor is not dependent on the location of a given field of view within the gel. Images taken before and after expansion of the same cell or group of cells were used to measure the ratio of length scales in the two images. **h.** Stacked-bar histogram showing the distribution of expansion factors in 58 gels across three plates. Expansion factors ranged from 3.5-5.1x across gels with an average of 4.16 +/- 0.394. Average expansion factors for each well plate: 3.78 +/- 0.171, 4.26 +/- 0.171, and 4.53 +/- 0.321.
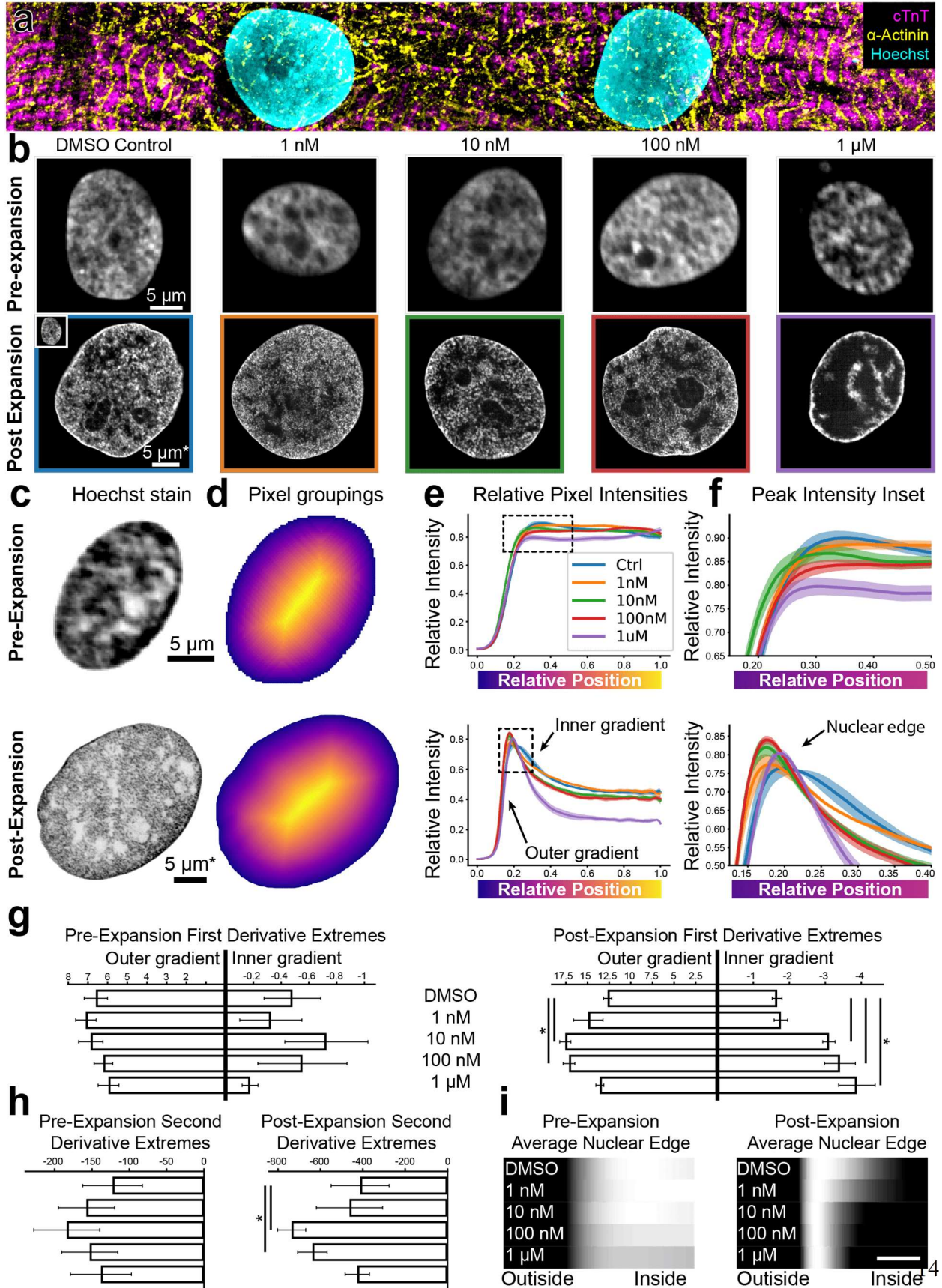
Fig. 3. HiExM shows altered nuclear morphology of cardiomyocytes treated with low doses of doxorubicin. a. hiPSC CMs imaged post-expansion in HiExM. **b.** Example images of hiPSC CM nuclei after dox treatment for 24 hrs. before (top) and after (bottom) expansion. *Scale bar represents biological scale assuming 4x expansion. **c.** Example images of hiPSC CM nuclei taken before (top) and after (bottom) expansion. **d.** Heatmaps of nuclei in **b** showing pixel groupings for subsequent analysis. These heatmaps are generated from the image mask after dilation, meaning that the outer edge represents a contour just beyond the nuclear periphery. **e.** Relative Hoechst intensity plotted as a function of pixel position relative to the edge of the dilated mask in pre- (top) and post- (bottom) expansion nuclei. Different curves represent dox concentrations, where Ctrl = DMSO control. Shaded regions represent SEM for n = 56, 71, 64, 92, and 62 nuclei in the pre-expansion case and n = 4 replicates in the expanded case. **f.** Insets of plots in **e** highlighting the nuclear periphery. **g.** Rate-of-change analysis of curves for pre- (left) and post- (right) expansion data. Outer edge values were taken as the maximum values of the derivatives for each condition, and inner edge values were taken as the minimum within the domain 0 - 0.4. **h.** Curvature analysis for pre- (left) and post- (right) expansion data. Values represent the minima of the second derivative for curves within the domain 0 – 0.4. **i.** Average Hoechst intensities plotted as gradients for each dox concentration. Scale bar represents 10 percent distance from the edge of the nucleus to the center. Error bars represent SEM as in **e**. * denotes significance from an independent two-sample t-test ($p < 0.05$).

MATERIALS AND METHODS

Cell culture

Human A549 cells were maintained in culture at a density between $2x10^3$ and $1x10^4$ cells/cm^2 in DMEM modified with 10% fetal bovine serum and 1% penicillin-streptomycin. Glass and plastic 96-well plates were seeded at ~$1x10^4$ and $7x10^4$ cells/cm^2 for expansion experiments.

Induced pluripotent stem cell-derived cardiomyocytes were purchased from Cellular Dynamics and cultured on glass-bottom 96-well plates at 30,000 cells/well. For drug treatment, CMs were plated on gelatin for 7 days (Cellular Dynamics) prior to drug treatment and incubated with Dox-containing media for 24 hours prior to fixation and subsequent sample preparation.

Immunofluorescence

Briefly, cells were fixed with 4% PFA for 15 minutes at room temperature and then blocked (1% bovine serum albumin and 0.1% Triton X100 in PBS) for one hour. Cells were then incubated for

15

one hour at 37˚C with primary antibodies in a blocking solution followed by incubation with secondary antibodies in blocking solution for one hour at 37 ˚C. Cells were washed between each stage in PBS three times at 0-, 5-, and 10-minute intervals.

Primary Antibodies	Vendor	Cat. Number
Monoclonal anti-alpha-Tubulin antibody	MilliporeSigma	T5168
Cardiac troponin T (TNNT2) Rabbit mAb	ABclonal	A4914
Monoclonal Anti-α-Actinin (Sarcomeric) antibody	MilliporeSigma	A7811
Secondary Antibodies	Vendor	Cat. Number
CF633 Chicken Anti-Mouse IgG (H+L)	Biotium	20222
CF568 Donkey Anti-Rabbit IgG (H+L)	Biotium	20098
Stains	Vendor	Cat. Number
Hoechst 33342	ThermoFisher Scientific	62249

HiExM Device Fabrication

HiExM devices were fabricated from polysulfone (McMaster-Carr 86735K74) using a Trak DPM2 CNC milling machine.

HiExM Workflow

Cells were fixed with 4% paraformaldehyde (PFA) and immunostained as described above and treated with Acryloyl-X, SE (6-((Acryloyl)amino)hexanoic acid, succinimidyl ester), abbreviated AcX (Invitrogen A20770), overnight at 4C. Cells were then washed twice with PBS, once with DI water, and the remaining liquid was gently aspirated from the wells. Gel solution composed of 4.04M sodium acrylate (AK Scientific R624), 0.506M acrylamide (MilliporeSigma A4058), 0.00934M n, n'-methylenebisacrylamide (MilliporeSigma M1533), 1.84M sodium chloride (Invitrogen AM9759) and 1.45X PBS 1mL (Invitrogen AM9625) was prepared in a light-protected tube. 1-[4-(2-Hydroxyethoxy)-phenyl]-2-hydroxy-2-methyl-1-propane-1-one (Irgacure 2959, MilliporeSigma 410896) was dissolved in DMSO at a concentration of 1.64M and this solution was mixed into the gel solution for a final Irgacure 2959 concentration of 0.0328M. The HiExM protocol was performed in a glove bag purged two times with dry nitrogen (MilliporeSigma Z530112). The gel solution was poured onto an absorbent pad to form a fluid reservoir. Devices

16

were dipped into the gel solution and immediately inserted into the well plate. The plate was then irradiated for 60 seconds with UVA light using a Uvitron Portaray curing lamp placed 20 inches beneath the plate (Uvitron International UV2270). Approximately 100 µL of Proteinase K (NEB P8107S) digestion solution was added to each gel-containing well and incubated for ~6 hours at room temperature. After digestion, Hoechst 33324 (Fisher scientific #62249) in DI water (1:5000 dilution) was added to wells for 5 minutes, then the 96-well plate was submerged in ~4 liters of DI water overnight under constant agitation while the gels were held in place by the device. Finally, the plate was removed from the water bath and devices removed from the well plate for imaging. For each well, excess water was aspirated and two drops of mineral oil was added to stabilize the expanded gel.

Image Acquisition

Confocal imaging was performed on an Opera Phenix imaging system (PerkinElmer). For NRR analysis, pre-expansion images were acquired with a 63x water objective (NA 1.15) in stacks of 6 planes spaced 0.5 microns apart and post-expansion images of the same plate were acquired using a 20x water objective (NA 1.0) in stacks of 50 planes spaced one micron apart. Prior to expansion, 61 tiled fields at the center of each well were imaged at 63x to capture cells that would be incorporated into the gel. After expansion, 12 fields in a cross pattern were imaged at 20x to capture a representative set of images for each gel across multiple wells. As a caveat, the centers of gels in HiExM should be avoided in imaging as they often include cells that are torn and disfigured due to the process of expansion detaching the gels from the device. Movies S1 and S2 were obtained on an EVOS M5000 epifluorescence microscope (ThermoFisher Scientific).

For cardiomyocyte experiments, images were acquired from 4 independent experiments. The sample sizes for each condition were as follows: 118, 111, 110, 113, and 77 cells for DMSO control, 1 nM, 10 nM, 100 nM, and 1 µM Dox, respectively across the four independent experiments.

Image analysis

Non-rigid registration

Non-rigid registration was performed to measure isotropic expansion within individual gels and across gels. For analysis represented in Fig. 2d, all fields of view were used in which a cell or group of cells could be identified in both the pre-expansion and the post-expansion image sets. The distance from the center of the analyzed field of view to the center of the well was measured

17

in the pre-expansion image set. For Fig. 2f, a single field of view near the periphery of the gel was arbitrarily chosen to represent the whole gel. Non-rigid registration was performed using a custom MATLAB analysis pipeline as described.[4] Briefly, pre and post expansion images are coarsely aligned using the TurboReg plugin for ImageJ.[14] This pair of outputs is then histogram normalized and masks are generated to exclude regions with no features by applying a gaussian blur. B-spline-based registration package in MATLAB was used to do non-rigid registration between the images. This procedure was done on image fields measuring 400px x 400px for all analyses.

The resulting data from a non-rigid registration analysis is a curve that represents measurement error as a function of measurement length. To synthesize these curves into single points (as represented in Figs. 2c-f), The average percent error up to 40 μm measurement length (as measured after expansion) was used. The average percent error was found as the mean of the ratios of error to measurement length for each individual data point in the error curve up to 40 μm measurement length.

Expansion Factor

To calculate expansion factors, images taken before and after expansion of the same cell or group of cells were compared. In both images, the distance between two easily identifiable features was measured manually in FIJI, and the ratio of those measurements was used to calculate the expansion factor.

Nuclear Periphery Analysis

Image stacks of Hoechst-stained nuclei were compiled and the midplane of each nucleus was manually identified as the half-way point between the bottom-most and top-most planes where the nucleus was in view. Midplane images were then manually thresholded to generated masks. These masks as well as their respective raw midplane images were then passed through a custom Python script to perform the analysis as follows: First, the mask was dilated to encompass a band of background signal outside of the nucleus. Second, the pixels at the edge of the mask were identified and their position and intensity information were stored. Third, pixels in the 4-neighborhood of each pixel from the outer-edge pixel group were identified and their position and intensity information stored (note that only pixels inside the boundary defined by the outer-edge pixel group were stored in this way). This third step was iterated for each new 'ring' until all pixels in the dilated mask were grouped. Finally, the mean pixel intensity values of each group were

taken and the list of mean values was run through linear interpolation to arrive at a list of length 500. To determine the inflection-point slopes of the resulting curves, the first derivative of each curve was taken using the finite difference approximation. To determine the curvature at the peak intensities of each curve, the second derivative was taken in the same way. Significance was determined from an independent two-sample t-test ($p < 0.05$).

Data Sharing Plans

Solidworks files for our devices as well as code for our analysis are available upon request.

Acknowledgements

Disclosures

ESB is an inventor on multiple patents related to expansion microscopy, and co-founder of a company exploring commercial applications of expansion microscopy. JHD, PM, CMDS, ALA, ESB, and LAB are inventors on a provisional patent filed for HiExM.